Editors' Suggestion | Featured in Physics

Giant and Controllable Photoplasticity and Photoelasticity in Compound Semiconductors

Jiahao Dong,[1,*] Yifei Li,[1,*] Yuying Zhou,[1,2] Alan Schwartzman,[1] Haowei Xu,[3] Bilal Azhar,[1] Joseph Bennett,[4] Ju Li,[1,3] and R. Jaramillo[1,†]

[1]*Department of Materials Science and Engineering, Massachusetts Institute of Technology, Cambridge, Massachusetts 02139, USA*
[2]*Shanghai Institute of Applied Physics, Chinese Academy of Sciences, Shanghai, 201800 China*
[3]*Department of Nuclear Science and Engineering, Massachusetts Institute of Technology, Cambridge, Massachusetts 02139, USA*
[4]*Department of Chemistry and Biochemistry, University of Maryland Baltimore County, Baltimore, Maryland 21250, USA*

(Received 5 November 2021; accepted 26 June 2022; published 3 August 2022)

We show that the wide-band gap compound semiconductors ZnO, ZnS, and CdS feature large photoplastic and photoelastic effects that are mediated by point defects. We measure the mechanical properties of ceramics and single crystals using nanoindentation, and we find that elasticity and plasticity vary strongly with moderate illumination. For instance, the elastic stiffness of ZnO can increase by greater than 40% due to blue illumination of intensity 1.4 mW/cm^2. Above-band-gap illumination (e.g., uv light) has the strongest effect, and the relative effect of subband gap illumination varies between samples—a clear sign of defect-mediated processes. We show giant optomechanical effects can be tuned by materials processing, and that processing dependence can be understood within a framework of point defect equilibrium. The photoplastic effect can be understood by a long-established theory of charged dislocation motion. The photoelastic effect requires a new theoretical framework which we present using density functional theory to study the effect of point defect ionization on local lattice structure and elastic tensors. Our results update the longstanding but lesser-studied field of semiconductor optomechanics, and suggest interesting applications.

DOI: 10.1103/PhysRevLett.129.065501

Introduction.—The literature on the interaction between light and the mechanical properties of semiconductors covers two distinct phenomena that have been more-or-less understood for decades: photostriction and photoplasticity. Photostriction occurs as illumination promotes electrons from the valence to the conduction band, thereby changing the cohesive energy and free volume of the crystal [1]. Photostriction can be calculated from thermodynamic coefficients, and typically has a small effect on the elastic modulus, although large effects have been reported [2,3]. Photoplasticity occurs as illumination changes the charge state of dislocations and point defects, thereby changing the force required for plastic deformation [4–9]. Photoplasticity is correlated with photoconductivity because deep levels that "store" charge, leading to persistent photoconductivity, can also contribute to dislocation pinning [4,6,10]. Giant photoplasticity has been reported in II-VI semiconductors; the magnitude of the photoplastic effect was brought into striking relief by a recent study of ZnS by Oshima *et al.* [11–15].

Large effects of illumination on elasticity—here termed *giant photoelasticity*—are less understood. Partially reversible elastic constant changes of up to 20% were reported in chalcogenide glasses and ascribed to photoinduced bond rearrangements [16,17]. Giant, reversible photoelasticity was reported based on nanoindentation measurements of ZnO and ZnS nanostructures and ascribed to surface photovoltage (SPV), and it is recognized that SPV can generate optomechanical response in polar crystals via the piezoelectric effect [2,13,17,18]. It is also well-known that illumination can toggle between bistable lattice configurations at deep levels, such as DX centers in III-V's, and negative-U centers in oxides and chalcogenides [19–23]. The connections between point defects, deep level ionization, local lattice distortion, illumination, and elasticity have yet to be studied.

Here we report giant and reversible photoplasticity and photoelasticity in CdS, ZnS, and ZnO. We measure optomechanical effects using nanoindentation combined with light illumination of variable intensity and wavelength. We find that optomechanical response can be tuned by sample processing, guided by principles of defect engineering. We use density functional theory (DFT) to study the effect of deep level ionization on elasticity, and we find a diversity of large effects that are semiquantitatively consistent with our experimental results. Our results illustrate the atomic origins of large optomechanical effects that remain little studied, but may be present in many compounds.

Methods.—We purchased samples from MTI Corp.: CdS single crystal, (0001) orientation; ZnS polycrystal, multispectral grade; ZnO single crystal, $(11\bar{2}0)$ orientation (a-plane). We measured samples as-received and after annealing at 500 °C for 120 h in a vacuum atmosphere

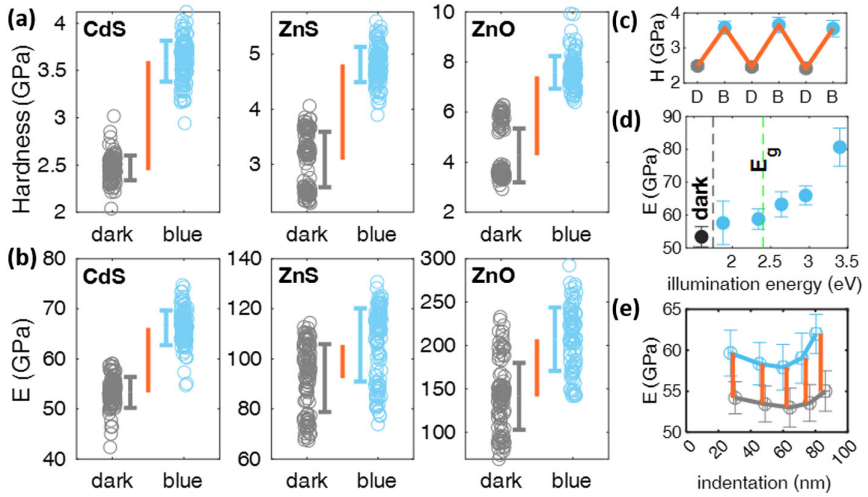

FIG. 1. Giant optomechanical effects in wide-band-gap II-VI compounds measured by nanoindentation. (a) Hardness and (b) Young's modulus (E) measured in the dark and under blue illumination by an LED with center wavelength 470 nm; irradiance at the sample surface is 1.4 mW/cm^2. The data shown include three successive cycles of darkness or illumination, and at each condition the measurement is repeated at 36 distinct locations, for a total of 108 separate measurements each for dark and illuminated conditions. The individual data are plotted directly; errorbarrs report average and standard deviation. Orange bars indicate the average change between dark and illuminated conditions. (c)–(e) Additional details provided for measurements on CdS. (c) Hardness during successive conditions of dark (D) and blue illumination (B). The data and error bars report the average and standard deviation of the 36 measurements performed at each condition; orange line traces the averages. (d) Dependence of E on the color of illumination, from red to uv; result of measurements in the dark are also shown. The irradiance is different for each condition: red $(660\ \text{nm}, 1.9\ \text{eV}) = 3.3\ \text{mW/cm}^2$; green $(530\ \text{nm}, 2.3\ \text{eV}) = 0.99\ \text{mW/cm}^2$; blue $(470\ \text{nm}, 2.6\ \text{eV}) = 1.4\ \text{mW/cm}^2$; violet $(420\ \text{nm}, 3.0\ \text{eV}) = 1.9\ \text{mW/cm}^2$; uv $(365\ \text{nm}, 3.4\ \text{eV}) = 22\ \text{mW/cm}^2$. (e) Depth dependence of the photoelastic effect, showing dark conditions (gray) and blue illumination (blue); illumination conditions are as in (a)–(c). Error bars on individual points represent the standard deviation of repeated measurements, and the solid lines are guides to the eye. The orange vertical bars indicate the photoelastic effect.

(CdS, ZnS, and ZnO, "ann. 1" below) and in a sulfur atmosphere (CdS and ZnS, "ann. 2" below). All samples were measured with as-delivered surfaces except for the vacuum-annealed ZnO, which we polished before measurement. We obtained a sample of ZnO with record-low defect density, made by homoepitaxial growth (film thickness 800 nm) with ozone-assisted molecular beam epitaxy [24]. We performed nanoindentation measurements using a Bruker Hysitron TriboIndenter 950, equipped with a standard diamond Berkovich tip. We performed measurements in two modes, high-speed indentation, and depth profiling. We illuminated samples during indentation using a custom-built illuminator.

We use DFT to study the contribution of point defect ionization and subsequent lattice relaxation to photoelasticity [25,26]. We simulate $2 \times 2 \times 2$, $2 \times 2 \times 3$, and $3 \times 3 \times 2$ CdS supercells with one sulfur atom removed in each case, corresponding to vacancy concentrations 6.25%, 4.17%, and 2.78%, respectively. An uncharged supercell, with no electrons removed, corresponds to a neutral vacancy ($V_S^{\times}$), whereas a supercell with two electrons removed corresponds to a doubly ionized vacancy ($V_S^{\bullet\bullet}$).

Results.—We find large and reversible photo hardening of CdS, ZnS, and ZnO. In Figs. 1(a) and 1(b) we present the hardness and Young's modulus (E) measured by nanoindentation in the dark and under blue illumination (470 nm, 1.4 mW/cm^2). Each dataset for a given illumination condition represents measurements at 108 distinct locations on the sample surface during successive cycles of light and dark conditions. In Fig. 1(c) we show the history dependence of hardness measured on CdS through multiple illumination cycles. CdS shows the largest and most repeatable optomechanical response. ZnS shows photohardening, but much smaller photo-elasticity than CdS. This is expected if sulfur vacancies are the source of giant photoelasticity, because multispectral ZnS is treated to improve optical transparency by reducing the sulfur vacancy concentration. However, despite the substantial dispersion in the measured data for ZnS, there is greater than 99% confidence that the dark and illuminated conditions have different elastic modulus (Student's $|t| = 6.6$). ZnO shows sizable photohardening and photoelasticity, but also shows the largest memory effect.

We find that the optomechanical effects increase as the illumination energy increases towards the band gap for all samples. In Fig. 1(d) we show the dependence of E measured on CdS with varying illumination wavelength: the photoelastic effect is finite but small for below-band gap light, then increases quickly for blue, violet, and uv illumination. This is evidence that the optomechanical

response is associated with carrier generation and trapping at defect levels. Depth-profile measurements reveal a nonmonotonic depth dependence of the photoelastic effect [Fig. 1(e)]. The effect is enhanced at larger indentation depth, which could result from interaction between charge trapping at point defects and an increasing concentration of dislocations, which may themselves be light sensitive, as are some screw dislocations in CdS [27]. Depth dependence may arise from interplay of nanoindentation geometry with nonisotropic photoelasticity. We also see a slight enhancement of photostiffening near the sample surface, which could result from stronger near-surface light absorption.

It is established that photoplasticity is related to photoconductivity by the interaction of dislocations with charge trapped at point defects [4,5]. Ionization of point defects associated with persistent photoconductivity is accompanied by substantial lattice relaxation; this was described for III-V semiconductors by Lang and Logan, later for ZnO, $CuInSe_2$, and $CuGaSe_2$ by Zhang, Wei, Zunger, and Lany, and more recently for CdS by ourselves [19,21–23]. These patterns of lattice relaxations create energy barriers that forestall carrier capture and recombination, so that photoexcitation produces persistent photoexcited ionized states. The effects of such lattice relaxations on elastic properties have not been studied, to our knowledge. We hypothesize that charge trapping at point defects under illumination is responsible for both photoplasticity and photoelasticity. To test this hypothesis, we anneal our samples to change point defect concentrations. We present our results in Fig. 2. We find that annealing reduces the photoplastic and photoelastic effects in all samples. These results confirm that the photoelastic effect can be controlled by materials processing, but do not yet directly confirm our hypothesis, because the defect concentrations remain unknown. Inductively coupled plasma optical emission spectroscopy (ICP-OES) measurements on CdS find an increase in S/Cd ratio upon annealing, changing from 0.958 ± 0.006 for the original sample, to 0.980 ± 0.001 and 0.976 ± 0.002 for the vacuum- and sulfur-annealed samples, respectively (error bars represent the statistical deviation of multiple measurements), consistent with our hypothesis. ICP-OES cannot measure intrinsic defect concentrations in ZnS and ZnO. As a further test, we measured the optomechanical response of homoepitaxial ZnO with record-low defect density [24]. We find that this nearly perfect ZnO has no optomechanical response, further supporting our hypothesis that photoplasticity and photoelasticity results from charge state transitions at point defects.

Next, we evaluate theoretical models to explain giant photoelasticity. We find that the local effects of lattice relaxation around ionized point defects are semiquantitatively consistent with the experimental observations. More conventional models of photostriction and the piezoelectric effect are not consistent with experiments.

We focus first on CdS, for which it is understood that charge trapping and lattice relaxation at sulfur vacancies is

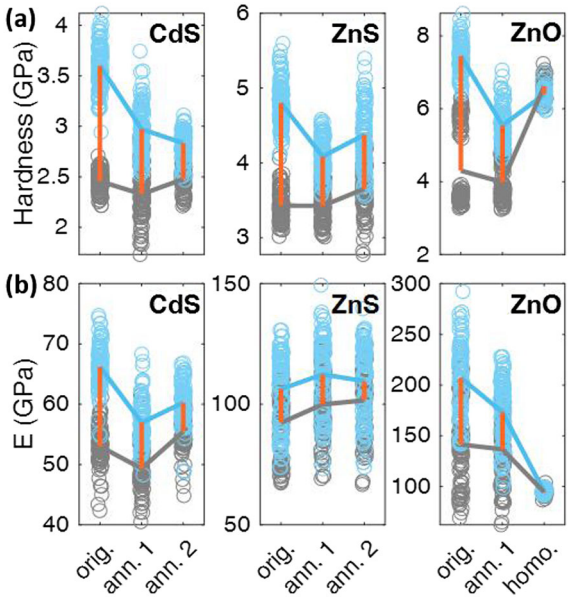

FIG. 2. Controlling giant optomechanical effects through sample processing. (a) Hardness and (b) Young's modulus (E) measured in the dark and under illumination by an LED for samples processed with different annealing conditions. Illumination conditions are the same as in Fig. 1. Gray and blue symbols indicate individual measurements taken during three successive dark or illumination cycles, totaling 108 separate measurements for each condition. Gray and blue lines trace the average for each condition, and the orange bars highlight the change upon illumination. The samples are labeled "orig." for the original, as-received samples, "ann. 1" for vacuum-annealed samples, "ann. 2" for sulfur-annealed samples, and "homo" for homoepitaxial ZnO.

responsible for persistent photoconductivity [23]. Sulfur vacancies are deep double donors occupied by two electrons at equilibrium ($V_S^{\times}$ in Kroger-Vink notation). Upon ionization, the lattice relaxes around the vacancy so as to raise the transition energy level close to the conduction band edge, converting the defect into a shallow donor; we have termed this defect-level switching [28]. In Figs. 3(a) and 3(b) we illustrate how the atomic lattice changes, first upon introduction of a neutral vacancy ($V_S^{\times}$), and then by vacancy ionization ($V_S^{\times} \rightarrow V_S^{\bullet\bullet}$). Upon introducing $V_S^{\times}$ we observe a peculiar pattern of lattice relaxation, whereby three of the Cd ions move inwards towards the vacancy, while one moves out [Fig 3(a)]. This three-in, one-out pattern can be reproduced with any one of three Cd ions directed mainly in the $\hat{a}$-$\hat{b}$ plane from the sulfur vacancy moving outward. However, the forth, directed along $\hat{c}$, cannot be made to relax outward. Even manually initiating the energy minimization with this forth ion displaced downward (in the view in Fig. 3) results in its relaxation inward, and the selection of a different ion to relax outward. For a simpler case we also model cubic ZnS. In Figs. 3(c) and 3(d) we illustrate the same sequence from the pristine lattice, to a neutral vacancy ($V_S^{\times}$), to an ionized vacancy

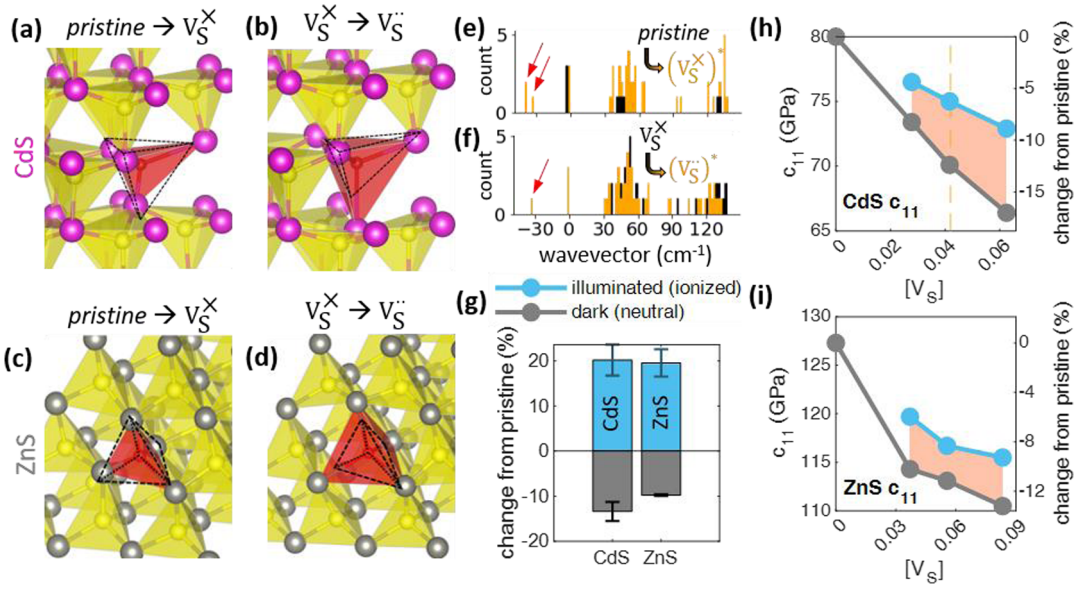

FIG. 3. Theoretical results for the change in the crystal lattice and elastic properties upon sulfur vacancy double ionization in CdS and ZnS. (a)–(b) Visualizing the lattice changes in CdS through the sequence: *pristine* → $V_S^\times$ → $V_S^{\bullet\bullet}$. Cd atoms shown in magenta, S shown in yellow; the missing sulfur atom and its coordination polyhedron are shown in red. (a) Change upon introducing a neutral sulfur vacancy. Black dashed line traces the Cd_4 tetrahedron in the pristine lattice, red polyhedron highlights the Cd_4 arrangement after introducing the vacancy and relaxing the lattice. (b) Change upon ionizing the sulfur vacancy. Black dashed line traces the Cd_4 tetrahedron in the lattice with neutral $V_S^\times$, red polyhedron highlights the Cd_4 arrangement after ionizing and relaxing the lattice. (c)–(d) As in (a)–(b), but for the case of ZnS; Zn atoms are shown in gray. (e)–(f) Γ-point phonon DOS presented as histograms; negative-frequency modes that drive lattice relaxation are indicated with red arrows. (e) Data for pristine CdS, and after creating a sulfur vacancy but before relaxing the lattice [indicated as excited state $(V_S^\times)^*$]. (f) Data for a relaxed lattice with a neutral vacancy, and after ionizing the vacancy but before relaxing the lattice [indicated as excited state $(V_S^{\bullet\bullet})^*$]. (g) Change in Cd-Cd and Zn-Zn distances around a sulfur vacancy, relative to the pristine lattice. Distances contract around $V_S^\times$ and expand around $V_S^{\bullet\bullet}$, as illustrated in (a)–(d). Error bars present the span of results calculated for varying [V_S], up to 6.25% and 8.33% missing sulfur atoms for the case of CdS and ZnS, respectively. (h) Change in c_{11} for neutral and doubly ionized vacancies in CdS, for a range of missing sulfur atoms fractions [V_S]. The photoelastic response is the difference between the neutral (gray, representing dark conditions) and ionized (blue, representing illuminated conditions) data, colored in orange. The orange dashed line marks [V_S] for the original CdS sample, determined by ICP-OES. (i) As in (h), but for the case of ZnS.

($V_S^{\bullet\bullet}$). We again observe a pattern of broken rotational symmetry around $V_S^\times$, with one Zn ion protruding. However, due to the higher symmetry of ZnS *vis-à-vis* CdS, any of the four Zn ions can be selected to protrude. These details pose interesting questions about how the three-in, one-out pattern manifests in real samples.

For a complementary view of the lattice instabilities and relaxation pathways, we analyze the phonon spectra. In Figs. 3(e) and 3(f) we present the zone center (Γ point) phonon density of states (DOS) of CdS in four cases, calculated from a $2 \times 2 \times 2$ supercell. In Fig. 3(e) we plot the spectra for a pristine lattice, and for the lattice after introducing a $V_S^\times$ site but before relaxation. The negative-frequency phonon modes signal the lattice instability. We observe two negative-frequency branches: a single mode at -33 cm^{-1} corresponding to an outward relaxation of the Cd ion directed along $\hat{c}$, and a degenerate mode at -39 cm^{-1} corresponding to outward relaxation of one of the other three Cd ions. This frequency splitting explains the observation, in our numerical experiments, that the three-in, one-out pattern always selects one of the three Cd ions mainly in the $\hat{a}$-$\hat{b}$ plane, but never the one directed along $\hat{c}$. The modes at -39 cm^{-1} correspond closely to the relaxation illustrated in Fig. 3(a).

In Fig. 3(f) we plot the spectra for a relaxed lattice with a $V_S^\times$ site, and for the lattice after ionizing but before relaxation. We observe one negative-frequency branch, which corresponds to the outward relaxation illustrated in Fig. 3(b). In this case there is no degeneracy, because the three-in, one-out pattern is already selected at the start of the simulation.

$V_S^\times \rightarrow V_S^{\bullet\bullet}$ ionization is accompanied by a large lattice relaxation in both CdS and ZnS. In Fig. 3(g) we quantify the change in Cd-Cd and Zn-Zn spacing relative to the pristine lattice, and we see that cation-cation distances change by more than 30% upon ionization. Because of these large lattice relaxations, the ionized state is metastable, with relaxation times on the order of 1 s or longer at room temperature for CdS. As a result even mild illumination can maintain a high fraction of defect ionization [23].

The large lattice relaxations are accompanied by large changes in the elasticity. In Figs. 3(h) and 3(i) we present the calculated c_{11} for varying $[V_S]$ for CdS and ZnS for the cases of neutral and ionized vacancies. Although introducing vacancies softens the lattice relative to the pristine case, the lattice then stiffens upon ionization $V_S^{\times} \rightarrow V_S^{\bullet\bullet}$: this is the photoelastic effect. DFT predicts a large photoelastic effect, on the order of 5% for the realistic $[V_S]$.

Summary.—We establish that giant photoelasticity is a generic phenomenon in common wide-band-gap compound semiconductors, and we show that both photoelasticity and photoplasticity can be tuned by materials processing. We demonstrate that the phenomena of ionization and lattice relaxation at point defects have substantial impacts on material elastic properties, far larger than the effects of photostriction and piezoelectricity. In the Supplemental Material we describe further the methods used, and present additional results and analysis [29–49].

Our results suggest future research into applications of giant optomechanics for structural metals, flexible electronics, and radiofrequency filters. We also anticipate further fundamental research into the nanomechanical properties of point defect transformations, including in lesser-studied semiconductors and in layered materials with highly anisotropic mechanical properties. There is an opportunity to advance DFT methods to more accurately model the elastic properties of crystals with neutral and ionized point defects. Orbital physics could help to explain trends in lattice relaxation; for instance, the three-in, one-out pattern observed here could result from a Jahn-Teller effect acting on cation molecular orbitals. There is also an open question of how the pattern of broken symmetry manifests across a population of defects. We hypothesize that long-range stress and strain fields can mediate interactions between the configurations of distant defects, producing an elastic tensor with symmetry distinct from the pristine crystal. Fields introduced during mechanical testing could similarly interact with point defect configurations, making the elastic tensor a dynamical field that interacts with both illumination and applied stress.

We acknowledge Brian Neltner, David Bono, Austin Akey, and Aubrey Penn for technical assistance. We acknowledge Joseph Falson and Masashi Kawasaki for providing a sample for study. We acknowledge illuminating discussion with Alexandru Georgescu. This work was supported by the Office of Naval Research MURI through Grant No. N00014-17-1-2661. We acknowledge use of the NanoMechanical Technology Laboratory in the Department of Materials Science and Engineering at MIT.

*These authors contributed equally to this work.
†rjaramil@mit.edu

[1] T. Figielski, Photostriction effect in germanium, Phys. Status Solidi **1**, 306 (1961).
[2] M. H. Zhao, Z.-Z. Ye, and S. X. Mao, Photoinduced Stiffening in ZnO Nanobelts, Phys. Rev. Lett. **102**, 045502 (2009).
[3] J. T. Lin, P. D. Shuvra, S. McNamara, H. Gong, W. Liao, J. L. Davidson, K. M. Walsh, M. L. Alles, and B. W. Alphenaar, Near-Surface Electronic Contribution to Semiconductor Elasticity, Phys. Rev. Applied **8**, 034013 (2017).
[4] Yu. A. Osip'yan and V. F. Petrenko, Nature of the photoplastic effect, Sov. J. Exp. Theor. Phys. **36**, 916 (1973).
[5] V. F. Petrenko and R. W. Whitworth, Charged dislocations and the plastic-deformation of II-VI compounds, Philos. Mag. A **41**, 681 (1980).
[6] Y. Osipyan, V. Petrenko, A. Zaretskii, and R. Whitworth, Properties of II-VI semiconductors associated with moving dislocations, Adv. Phys. **35**, 115 (1986).
[7] T. Garosshen, C. Kim, and J. Galligan, On the influence of light on dislocation-motion in compound semiconductors, J. Electron. Mater. **19**, 889 (1990).
[8] L. Carlsson, Orientation and temperature dependence of the photoplastic effect in ZnO, J. Appl. Phys. **42**, 676 (1971).
[9] L. Carlsson and C. Svensson, Photoplastic effect in ZnO, J. Appl. Phys. **41**, 1652 (1970).
[10] R. H. Bube, *Photoconductivity of Solids* (Wiley, New York, 1960).
[11] B. Wolf, A. Belger, D. C. Meyer, and P. Paufler, On the impact of light on nanoindentations in ZnSe, Phys. Status Solidi A **187**, 415 (2001).
[12] B. Wolf and A. Richter, The concept of differential hardness in depth sensing indentation, New J. Phys. **5**, 15 (2003).
[13] X. J. Zheng, G. C. Yu, Y. Q. Chen, S. X. Mao, and T. Zhang, Photoinduced stiffening and photoplastic effect of ZnS individual nanobelt in nanoindentation, J. Appl. Phys. **108**, 094305 (2010).
[14] Y. Wei, L. H. Xu, Y. W. Tao, X. J. Zheng, J. H. Yang, D. F. Zou, and S. X. Mao, Width-to-thickness ratio dependence on photoplastic effect of ZnS nanobelt, Appl. Phys. Lett. **101**, 091904 (2012).
[15] Y. Oshima, A. Nakamura, and K. Matsunaga, Extraordinary plasticity of an inorganic semiconductor in darkness, Science **360**, 772 (2018).
[16] K. Tanaka, N. Kawakami, and A. Odajima, Photoinduced elastic changes in amorphous As2S3 films, Jpn. J. Appl. Phys. **20**, L874 (1981).
[17] K. Tanaka, Reversible photostructural change: Mechanisms, properties and applications, J. Non-Cryst. Solids **35–36**, 1023 (1980).
[18] J. Lagowski and H. C. Gatos, Photomechanical effect in noncentrosymmetric semiconductors-CdS, Appl. Phys. Lett. **20**, 14 (1972).
[19] D. V. Lang and R. A. Logan, Large-Lattice-Relaxation Model for Persistent Photoconductivity in Compound Semiconductors, Phys. Rev. Lett. **39**, 635 (1977).
[20] P. M. Mooney, Deep donor levels (DX Centers) in III-V semiconductors, J. Appl. Phys. **67**, R1 (1990).
[21] S. B. Zhang, S.-H. Wei, and A. Zunger, Intrinsic N-type versus p-type doping asymmetry and the defect physics of ZnO, Phys. Rev. B **63**, 075205 (2001).
[22] S. Lany and A. Zunger, Anion vacancies as a source of persistent photoconductivity in II-VI and chalcopyrite semiconductors, Phys. Rev. B **72**, 035215 (2005).

[23] H. Yin, A. Akey, and R. Jaramillo, Large and persistent photoconductivity due to hole-hole correlation in CdS, Phys. Rev. Mater. **2**, 084602 (2018).
[24] J. Falson, Y. Kozuka, M. Uchida, J. H. Smet, T. Arima, A. Tsukazaki, and M. Kawasaki, MgZnO/ZnO heterostructures with electron mobility exceeding 1×106 Cm2/Vs, Sci. Rep. **6**, 26598 (2016).
[25] G. Kresse and J. Furthmüller, Efficient iterative schemes for Ab Initio total-energy calculations using a plane-wave basis set, Phys. Rev. B **54**, 11169 (1996).
[26] G. Kresse and J. Furthmüller, Efficiency of Ab-Initio total energy calculations for metals and semiconductors using a plane-wave basis set, Comput. Mater. Sci. **6**, 15 (1996).
[27] A. A. Istratov and O. F. Vyvenko, DX-like center generated by uniaxial strains of screw dislocations in CdS, J. Appl. Phys. **80**, 4400 (1996).
[28] H. Yin, A. Kumar, J. M. LeBeau, and R. Jaramillo, Defect-Level Switching for Highly Nonlinear and Hysteretic Electronic Devices, Phys. Rev. Applied **15**, 014014 (2021).
[29] A. C. Fischer-Cripps, *Nanoindentation*, 2nd ed. (Springer-Verlag, New York, 2004).
[30] W. Kohn and L. J. Sham, Self-consistent equations including exchange and correlation effects, Phys. Rev. **140**, A1133 (1965).
[31] P. Hohenberg and W. Kohn, Inhomogeneous electron gas, Phys. Rev. **136**, B864 (1964).
[32] J. P. Perdew, K. Burke, and M. Ernzerhof, Generalized Gradient Approximation Made Simple, Phys. Rev. Lett. **77**, 3865 (1996).
[33] Y. Le Page and P. Saxe, Symmetry-general least-squares extraction of elastic data for strained materials from Ab Initio calculations of stress, Phys. Rev. B **65**, 104104 (2002).
[34] X. Wu, D. Vanderbilt, and D. R. Hamann, Systematic treatment of displacements, strains, and electric fields in density-functional perturbation theory, Phys. Rev. B **72**, 035105 (2005).
[35] G. Makov and M. C. Payne, Periodic boundary conditions in Ab Initio calculations, Phys. Rev. B **51**, 4014 (1995).
[36] J. Neugebauer and M. Scheffler, Adsorbate-substrate and adsorbate-adsorbate interactions of Na and K adlayers on Al(111), Phys. Rev. B **46**, 16067 (1992).
[37] A. Walsh, Correcting the corrections for charged defects in crystals, npj Comput. Mater. **7**, 72 (2021).
[38] P. Giannozzi *et al.*, QUANTUM ESPRESSO: A modular and open-source software project for quantum simulations of materials, J. Phys. Condens. Matter **21**, 395502 (2009).
[39] P. Giannozzi *et al.*, Advanced capabilities for materials modelling with quantum ESPRESSO, J. Phys. Condens. Matter **29**, 465901 (2017).
[40] A. Kokalj, XCrySDen—A new program for displaying crystalline structures and electron densities, J. Mol. Graphics Modell. **17**, 176 (1999).
[41] X. Fu *et al.*, Tailoring exciton dynamics by elastic strain-gradient in semiconductors, Adv. Mater. **26**, 2572 (2014).
[42] K. Nishidate, T. Sato, Y. Matsukura, M. Baba, M. Hasegawa, and T. Sasaki, Density-functional electronic structure calculations for native defects and Cu impurities in CdS, Phys. Rev. B **74**, 035210 (2006).
[43] H. H. Woodbury, Diffusion of Cd in CdS, Phys. Rev. **134**, A492 (1964).
[44] J. S. McCloy, W. Wolf, E. Wimmer, and B. J. Zelinski, Impact of hydrogen and oxygen defects on the lattice parameter of chemical vapor deposited zinc sulfide, J. Appl. Phys. **113**, 023706 (2013).
[45] N. Hernandez-Como, V. Martinez-Landeros, I. Mejia, F. S. Aguirre-Tostado, C. D. Nascimento, G. de M. Azevedo, C. Krug, and M. A. Quevedo-Lopez, Defect control in room temperature deposited cadmium sulfide thin films by pulsed laser deposition, Thin Solid Films **550**, 665 (2014).
[46] L. J. Brillson, Surface photovoltage and auger spectroscopy studies of $(11\bar{2}0)$ CdS surface, J. Vac. Sci. Technol. **12**, 249 (1975).
[47] S. Simov, M. Kalitzova, E. Nikolova, and I. Baltov, Surface photovoltage spectroscopy study of CdS thin films, Surface Sci. **59**, 115 (1976).
[48] D. Berlincourt, H. Jaffe, and L. R. Shiozawa, Electroelastic properties of the sulfides, selenides, and tellurides of zinc and cadmium, Phys. Rev. **129**, 1009 (1963).
[49] See Supplemental Material at http://link.aps.org/supplemental/10.1103/PhysRevLett.129.065501 for further details on the methods used, and additional results and analysis.

SUPPLEMENTAL MATERIAL: Giant & controllable photo-plasticity and photo-elasticity in compound semiconductors

Yifei Li,[1†] Jiahao Dong,[1†] Yuying Zhou,[1,2] Alan Schwartzman,[1] Haowei Xu,[3] Bilal Azhar[1], Joseph Bennett,[4] Ju Li,[1,3] R. Jaramillo[1*]

1. Department of Materials Science and Engineering, Massachusetts Institute of Technology, Cambridge, MA 02139 USA

2. Shanghai Institute of Applied Physics, Chinese Academy of Sciences, Shanghai, 201800 China

3. Department of Nuclear Science and Engineering, Massachusetts Institute of Technology, Cambridge, MA 02139 USA

4. Department of Chemistry & Biochemistry, University of Maryland Baltimore County, Baltimore, MD 21250

† Equally-contributing authors

* rjaramil@mit.edu

S1. Experimental methods, extended presentation

We performed nanoindentation measurements using a Bruker Hysitron TriboIndenter 950, equipped with a standard diamond Berkovich tip. We performed measurements in two modes, high speed indentation and depth profiling (XPM and CMX, respectively, in the manufacturer's terminology). We determined sample hardness and reduced modulus using the Oliver-Pharr method [29]. We calculated the sample Young's modulus from the reduced modulus using Poisson ratios of 0.346, 0.327, and 0.225 for CdS, ZnO, and ZnS, respectively, together with the properties of the diamond indenter (elastic modulus = 1140 GPa, Poisson ratio 0.07).

We illuminated samples during indentation using a custom-built illuminator with light-emitting diodes (LEDs) with center wavelengths 660, 530, 470, 420, and 365 nm; the first four are LUXEON Z LEDs integrated on a Saber Z4 color mixing array (LuzeonStarLEDs) used without a lens, and that at 365 nm is a LZ1-00UV00 (Osram/LEDEngin) used with a lens. We measured the illumination intensity at the sample position using a calibrated Si diode, both with the diode installed on the instrument stage with an appropriate aperture, and with benchtop measurements; the intensity values reported here are averages of multiple such measurements.

We measured the composition of CdS by inductively coupled plasma optical emission spectroscopy (ICP-OES) using an Agilent ICP-OES VDV 5100 spectrometer, operated in the radial configuration. We prepared calibration standards of 500 and 750 µg/ml for cadmium and sulfur, respectively, by diluting 1000 µg/ml single-element standards of each element (Inorganic Ventures) with 2% HNO_3. We prepared aqueous solutions of the samples by adding 40 mg of sample powder to 1 mL of 68% HNO_3 and heating on a hotplate at 70 ˚C until the solution was clear, before diluting to 2% HNO_3 with deionized water. We filtered all standards and samples with a 0.2 µm filter.

Samples for transmission electron microscopy (TEM) were prepared following standard lift-out techniques, using a Helios 660 Dual Beam FIB/SEM. Surface damage and Ga implantation were removed using a Fischione Nanomill 1040 Ar-ion mill. TEM imaging and diffraction were performed on a Thermo Fisher Themis Z G3 60-300 kV (scanning) transmission electron microscope operated at 200 kV. Selected area electron diffraction (SAED) patterns were collected with parallel illumination on the Ceta CMOS camera. A 10 um objective aperture was used for bright field and "dirty" dark field imaging.

S2. Theoretical and computational methods, extended presentation

To study the contribution of point defect ionization and subsequent lattice relaxation to photo-elasticity, we use density function theory (DFT) calculations performed using the Vienna ab-initio simulation package (VASP), version 5.4 [25,30,31]. We treat the core and valence electrons by the projector-augmented plane-wave method, and we approximate the exchange-correlation interaction by the generalized gradient approximation functional, implemented in the Perdew-Burke-Ernzerhof form [32]. The energy minimization and force convergence criteria are 10^{-7} eV and 10^{-3} eV/Å, respectively. The k-mesh are chosen so that the product of the lattice constant and the number of k-points is larger than 30 Å. We simulate $2 \times 2 \times 2$, $2 \times 2 \times 3$, and $3 \times 3 \times 2$ wurtzite CdS supercells with one sulfur atom removed in each case, corresponding to vacancy concentrations 6.25%, 4.17%, and 2.78%, respectively. We also simulate $3 \times 3 \times 3$ zincblende ZnS and CdS supercells with one sulfur atom removed, corresponding to vacancy concentrations 3.70%. An uncharged supercell, with no electrons removed, corresponds to a neutral vacancy ($V_S^{\times}$), whereas a supercell with two electrons removed corresponds to a doubly-ionized vacancy ($V_S^{\cdot\cdot}$). We mechanically relax the supercells using the conjugated gradient (CG) algorithm. In each case, we calculate elastic stiffness tensors after relaxation, and phonon modes by the finite-difference method [33,34].

To simulate the ionized defects in the supercell, we reduce the total electron number of the system, using NELECT tag provided by VASP. The simple approach works because the two electrons trapped at $V_S^{\times}$ have the highest and next-to-highest energy in the system, and DFT converges to the lowest system energy. We confirm the change in defect charge state by plotting the electron localization function.

Changing the total electron count in the supercell creates two practical issues in the calculation. First, the long-range Coulomb interaction between charged defects diverges under periodic boundary conditions. To address this, a homogenous ("jellium") background charge is introduced to enforce overall charge neutrality and ensure convergence of the total energy. The second issue is the shifting of the total energy. The DFT calculation includes the interactions between charged defects and the jellium background. We want to subtract these unphysical interactions because the charged defects are not in reality periodic, and the jellium background is an artifact introduced for computational convenience. VASP uses several terms to correct the total energy. The leading term $\frac{e^2 q^2 \alpha}{L\varepsilon}$ describes the interactions between periodic charged defects, where q is the net charge, L is

the supercell size, α is the Madelung constant and ε is the dielectric constant. Higher terms describe the interaction between the charged defects and jellium background, and the interaction of the jellium background with itself [35,36].

These currently-available and widely-used methods of calculating the total energy of a charged supercell still suffer from systematic errors [37]. Nevertheless, we claim that these errors do not strongly affect the calculated elastic moduli, since the errors depend mainly on supercell size, and are relatively insensitive to small reconfigurations of the atomic lattice.

Since the introduction of vacancies breaks the symmetry of the pristine lattice, stiffness tensor elements that are equivalent for the pristine crystal may develop slight differences. We therefore remove the sulfur atom at high-symmetry position and average the stiffness tensor elements according to the hexagonal or cubic symmetry of the pristine crystal, to produce estimates that can be more directly compared with experiments. We found that the elasticity calculation results depend on the energy cutoff used during convergence testing; for consistency, we use 520 eV as cutoff energy for all calculations.

Accompanying this manuscript is a movie file ("CdS 2x2x2 ionization movie.mpg") visualizing the lattice relaxation following sulfur vacancy ionization in CdS ($V_S^{\times} \rightarrow V_S^{\cdot\cdot}$), produced from the lattice relaxation process calculated in DFT for a $2 \times 2 \times 2$ wurtzite supercell. To simulate the lattice relaxation, we use Quantum Espresso (QE) package, which is based on DFT and plane-wave sudopotential method, and we use XCrySDen to convert the trajectory of lattice relaxation into a movie [38–40]. In the movie, the direction and length of green arrows represent the direction and strength of the instantaneous force applied on each atom.

To quantify photostriction, we use a model describing the effect of strain gradients on exciton concentration (*i.e.* an exciton funnel) as described by Fu *et al.* [41]:

$$\nabla\left(D\nabla n - \mu n \nabla E_g\right) = g(r) - \frac{n}{\tau} \qquad \text{(Eq. 1)}$$

n is the exciton concentration; μ is the carrier mobility (we use $\mu = 150$ cm^2/V·s); $D = \mu k_B T$ is the diffusivity; $g(r)$ is the optical generation rate, estimated by the illumination intensity of 1.5 mW/cm^2 corresponding to the blue LED (470 nm) and the finite absorption length at this wavelength; $\tau = 200$ ps is the excited-state lifetime; this can vary by many orders-of-magnitude without affecting our results. The strain gradient $\nabla\epsilon$ creates a band gap gradient ∇E_g via the coefficient $\mathrm{d}E_g/\mathrm{d}\varepsilon$. We estimate $\nabla\epsilon$ using a circularly-symmetric model of nanoindentation, and we calculate $\mathrm{d}E_g/\mathrm{d}\varepsilon$ using DFT. We numerically solve the generation-drift-diffusion-recombination equation (Eq. 1) using MATLAB. The details of the strain gradient $\nabla\epsilon$ during nanoindentation requires finite-element analysis. We simplify by assuming that the gradient is circularly-symmetric around the tip, equal to 0.002 nm^{-1} within a radius of 50 nm from the tip, and 0 outside of this radius. We estimate $\mathrm{d}E_g/\mathrm{d}\varepsilon$ by using DFT to calculate E_g of the structures under varying uniaxial strain along the principal axes, and averaging over orientation. By solving Eq.1,

we estimate the exciton concentration accumulated immediately below and around the nanoindentation tip.

S3. Depth profiling measurements, extended presentation

The Young's modulus can be measured as a function of indentation load (or depth) by superimposing a small oscillatory load on top of the quasi-static load during indentation, and continuously measuring the oscillatory response during indentation. These measurements further distinguish photoelasticity from photoplasticity, and provide insight into the depth-dependence of photoelasticity, including the influence of near-surface optical absorption, and the effects of plastic deformation and dislocation generation during indentation. In **Fig. S1a** we reproduce from **Fig. 1e** the depth-dependent results measured on the original (*i.e.*, non-annealed) CdS sample. The photoelastic response measured is quantitatively similar to that measured by discrete nanoindentations (**Fig. 1b**), but additionally reveals a non-monotonic depth dependence, as discussed in the main text. In **Fig. S1b** we quantify the photo-stiffening as a function of depth.

There is a slight leftward shift of the position on moving from the dark to the light measurements, for each nominal depth, visible in **Fig. S1a**. This is because the depth-dependent measurements are load-controlled. The photostiffening effect means that a given force will result in a shallower depth under illumination compared to in the dark. This explains the shift.

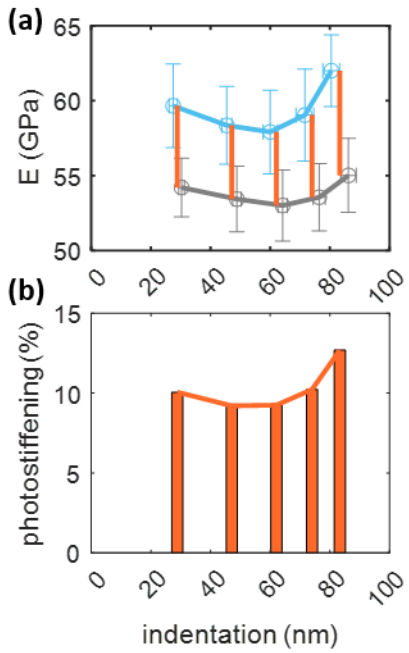

Figure S1: Measuring the photoelastic effect for varying indentation depth. Sample is the same non-annealed CdS as in **Fig. 1**. (a) Measurements in the dark (grey) and with blue light illumination (blue); data reproduced from **Fig. 1e**, illumination conditions are the same as in **Fig. 1a-c** and **Fig. 2**. The error bars on individual points represent the standard deviation of repeated measurements, and the solid lines are guides to the eye. The orange

vertical bars indicate the photoelastic effect. The dark and illuminated data series are not measured at exactly the same indentation values because the measurements are load-controlled, not displacement-controlled. (b) Results from (a) presented as photostiffening (% change relative to dark values).

S3. Memory effect and photoelastic response time

In **Fig. 1c** we presented the change in hardness of CdS during three dark / blue illumination cycles. In **Fig. S2a** we reproduce this data for CdS, and also present data for ZnS and ZnO. The data separated by illumination cycle in **Fig. S2a** is the same that is grouped by illumination condition in **Fig. 1a**. Of these three materials, CdS has the most repeatable optomechanical response, whereas ZnO has the largest memory effect.

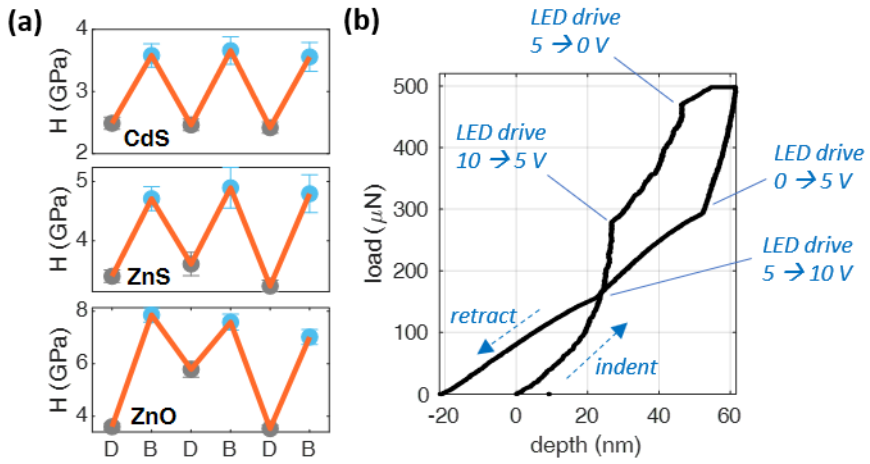

Figure S2: Evidence for fast and slow optomechanical response. (a) Hardness during successive conditions of dark (D) and blue illumination (B). The data and error bars report the average and standard deviation of the 36 measurements performed at each condition; orange line traces the averages. Data for CdS is reproduced from **Fig. 1c**. (b) Load-displacement data measured during a single, quasi-static nanoindentation on CdS with changing illumination. The illumination is indicated by the LED drive voltage, and changes in the sequence: 10 V → 5 V → 0 V → 5 V → 10 V, as indicated in the figure.

It is likely that materials exhibiting giant optomechanical response have both fast and slow components, as is typical for photoconductivity [23]. Our nanoindentation measurements are not designed to measure temporal response, and we can only place approximate bounds on the response times. The data in **Fig. S2a** suggest that the slow response of CdS is not slower than the time between measurement conditions, approximately 15 – 20 minutes. ZnS and ZnO do appear to have some response slower than this. The fast response is faster than the point-to-point measurement time. This can be illustrated by changing the illumination during individual indentations. In **Fig. S2b** we show data for an indentation on CdS during which the blue light illumination was cycled. The indentation begins with the light at full intensity (drive voltage 10 V, intensity 1.4 mW/cm^2). When the drive is stepped down to 5 V (intensity 0.92 mW/cm^2), and again

to 0 V, the material becomes more compliant, as expected from our other measurements. On the timescale of the nanoindentation measurements, the material response appears to be instantaneous. During withdrawal the light is turned on again, first to 5 V, and then to 10 V. Increasing the illumination intensity makes the material stiffer, causing a rapid decrease in indentation depth (the measurements are load-controlled), again on a time scale faster than the measurement. The point-to-point measurement time during quasi-static nanoindentation is approximately 100 ms, so we conclude that the sample fast response is faster than this. We note that, while interesting, measurements with variable illumination during individual indentations (as in **Fig. S2b**) are not advisable for accurate measurements of mechanical property changes with illumination. The data cannot be analyzed with the accepted Oliver-Pharr method. Further, we find that changing illumination produces transients in the instrument response, possibly due to some heating of the apparatus. Therefore, for all data presented here (except for **Fig. S2b**), we allow a refractory period to elapse between changing illumination and nanoindentation.

S4. Control of point defect concentrations by annealing

Most real-world samples of most compound semiconductors – and particularly those with volatile anions, such as sulfides and oxides – are far-from-equilibrium. Under Cd-rich conditions (which favor sulfur vacancies), the formation energy $\Delta E^{\text{Cd-rich}}(\text{V}_\text{S}) \approx 0.75$ eV; under S-rich conditions (which suppress sulfur vacancies), this energy is $\Delta E^{\text{S-rich}}(\text{V}_\text{S}) \approx 2.1$ eV [42]. This means that, at room temperature, the fractional vacancy occupation ought to be in the range $5.2 \times 10^{-36} - 2.5 \times 10^{-13}$ (we neglect entropic factors, which modify the results only a little). At the annealing temperature of 500 °C, this range is $1.3 \times 10^{-5} - 2.0 \times 10^{-14}$.

The chemical analysis of the original CdS single crystal suggests a S/Cd ratio of 0.958 ± 0.006. Our microscopy demonstrates that the samples are indeed single-crystals, without evidence of secondary phases or grain boundaries. Therefore, the non-stoichiometry is accommodated within the crystal lattice. It is known from theory and experiment that cadmium interstitials are particularly unlikely in CdS, so the off-stoichiometry can be assigned mainly to sulfur vacancies [42,43]. In **Fig. S3** we illustrate this far-from-equilibrium condition as a plot of

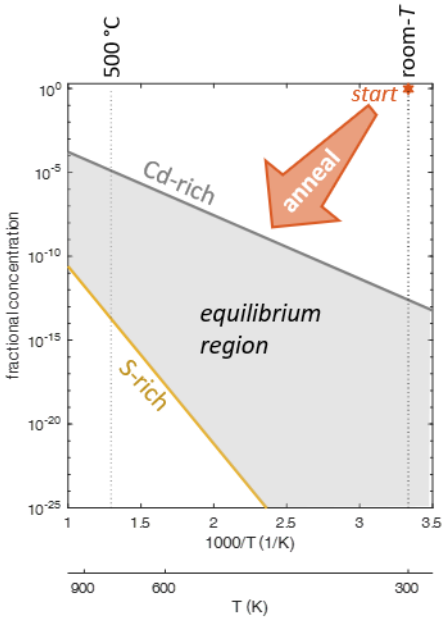

$[V_S]$ *vs*. temperature. This plot illustrates that annealing is likely to reduce $[V_S]$ for all annealing conditions.

Figure S3: Fraction of vacant sulfur sites at equilibrium, computed from calculated formation energies for Cd-rich and S-rich conditions. The as-grown CdS crystal has a sulfur vacancy concentration far above equilibrium (indicated with red star). Annealing therefore is likely to reduce $[V_S]$ for all annealing conditions.

We do observe that annealing brings the S/Cd ratio closer to unity, in agreement with expectations from equilibrium thermodynamics. There remains the puzzle over why S/Cd ends up slightly higher for vacuum annealing (S/Cd = 0.980 ± 0.001) than for sulfur atmosphere annealing (S/Cd = 0.976 ± 0.002). We first note that these numbers are almost quantitatively consistent with each other, the error bars being the standard deviation of repeated measurements. However, we also propose a mechanism by which the vacuum annealing process may approach equilibrium faster than the sulfur annealing process. It has long been considered that the dominant intrinsic point defects in CdS is the sulfur vacancy, and that sulfur vacancies accelerate both Cd and S diffusion [43]. Reducing $[V_S]$ thereby slows the rate at which the Cd lattice - therefore the crystal as a whole – approaches equilibrium.

Analytical measurement of intrinsic point defect concentrations in compound semiconductors are notoriously challenging and usually unavailable. This is especially so for compounds of volatile and relatively light elements, such as S and O. In this study, we were able to analyze Cd:S atomic ratios by ICP-OES, because the acid digestion process for CdS is well-established, and reliable standards are commercially available. Unfortunately, the digestion process is not well-established for ZnS, and our efforts to measure Zn:S atomic ratios by ICP-OES were unsuccessful; and, obviously, measuring the Zn:O ratio in ZnO crystals is not possible by ICP analysis of aqueous solutions.

Diffraction analysis can occasionally be used to infer point defect concentrations, but unfortunately here is not particularly useful. In **Fig. S4** we present X-ray diffraction (XRD) data measured on our samples before and after annealing. The data on CdS and ZnS illustrate lattice constant changes with annealing. For the case of CdS, it appears that annealing makes the sample inhomogeneous, presumably with a diffusion gradient from the free surfaces into the bulk. Unfortunately, there is no clear interpretation of the data in terms of point defect concentrations. For the case of ZnS, one theoretical study suggests volume contraction with sulfur vacancy concentration, and no clear experimental reports are available [44]. This would suggest that the reduction in lattice constant upon annealing, observed here, results from a reduction in sulfur vacancy concentration. This is consistent with our interpretation, but is far from settled. For the case of CdS, there is one published study that correlates electronic transport properties (*i.e*., carrier concentration, mobility, and resistivity) with the lattice constant [45]. These results suggest an increase in lattice constant with an increase in defect concentration; the connection to sulfur vacancies comes only by assuming them to be the dominant electron donors, which is a tenuous assumption. This would suggest that the increase in lattice constant upon annealing, observed here, results from a reduction in sulfur vacancy concentration. Again, this is consistent with our interpretation, but is far from settled.

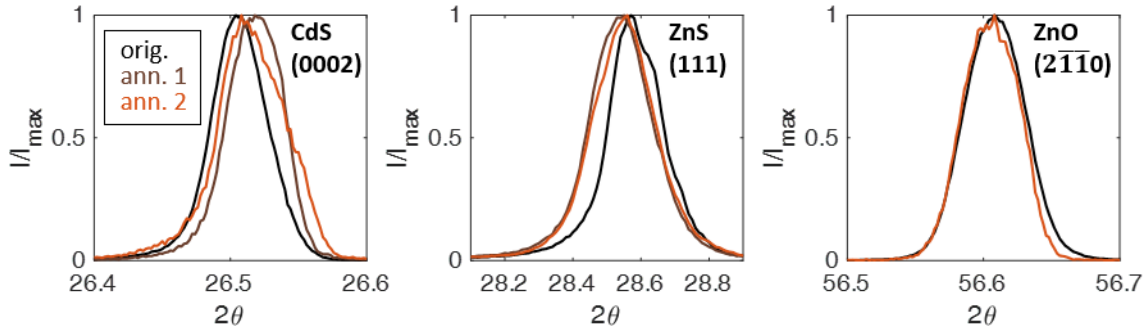

Figure S4: XRD data (Cu K-α) measured on samples before and after annealing; colors are as labeled in (a).

A further complication in the analysis of the effect of point defect concentrations on optomechanics is the presence of multiple length scales. Annealing at 500 ℃ for 120 h may affect composition to a depth greater than 1 μm from the sample surfaces, although estimates range from 10 nm to 100 cm because the self-diffusion coefficients at 500 ℃ are not well characterized. Nanoindentation measures mechanical properties to a depth of ~100 nm. The depth of illumination varies with wavelength and material, from over 1 μm to under 50 nm for the experiments reported here. Our XRD measurements using Cu K-α radiation are sensitive to the topmost ~10 μm of the sample, and the CdS XRD data suggest that annealing produces a non-uniform composition within this length scale. To more directly study the depth-dependent properties we carried out electron diffraction measurements in the TEM in cross-section geometry. In **Fig. S5** we present diffraction data measured at two distances from the surface for all three CdS samples: approximately 100 nm from the surface ("near-surface"), and between 2 - 3 μm from the surface ("bulk"). We see no clear trends in the lattice spacing upon comparing the near-surface and the bulk, and upon comparing the electron diffraction and the XRD data. The lattice spacing changes due to annealing that are apparent in the CdS XRD data are on the order of 0.05%, which is too fine to resolve in electron diffraction. The electron diffraction data do however confirm the single-crystalline and single-phase nature of the samples.

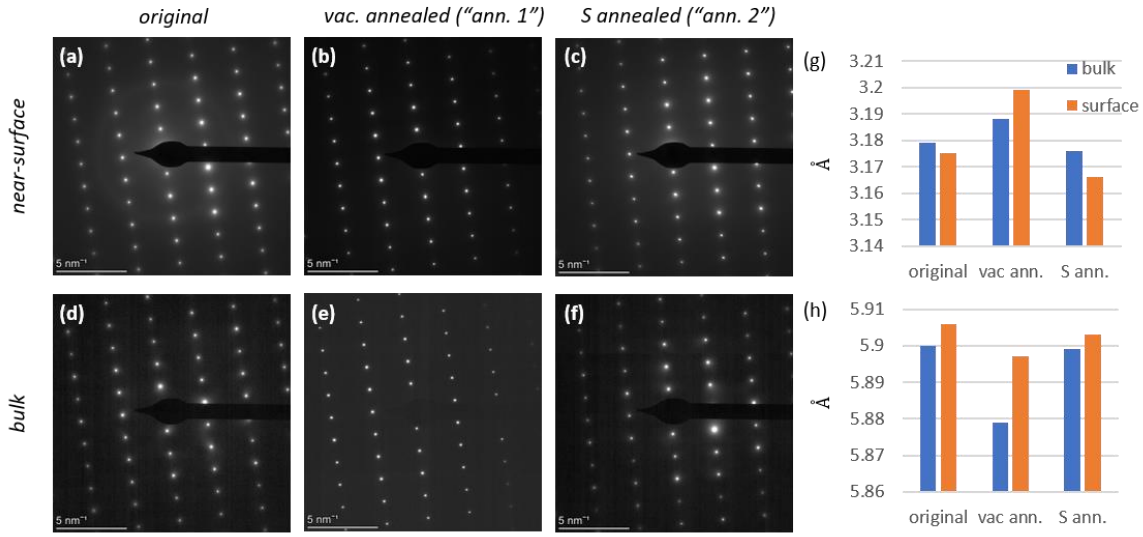

Figure S5: Electron diffraction data measured "near-surface" (a-c) and in the "bulk" (d-f) for the three CdS samples studied here. Near-surface data is measured approximately 100 nm from the surface; bulk data is measured between 2 – 3 μm from the surface. There are no clear trends in lattice spacing upon comparing the near-surface and bulk data, as shown in the d-spacing analysis (g-h).

S5. Effect of annealing on extended defect concentrations

In **Fig. S6** we present TEM micrographs measured on the three CdS samples, to better understand the effects of annealing on extended defects. These data illustrate that the original sample (**Fig. S6a**) is a uniform single-crystal, nearly free of dislocations and other extended defects. The annealing processes introduce interesting patterns of extended defects. The vacuum-annealed sample ("ann. 1", **Fig. S6b**) appears to have developed a series of defects extending from the surface directly into the sample, although their cause is unknown. The sulfur-annealed sample ("ann. 2", **Fig. S6c**) developed a series of screw dislocations, oriented parallel to the surface, and distributed uniformly and at random.

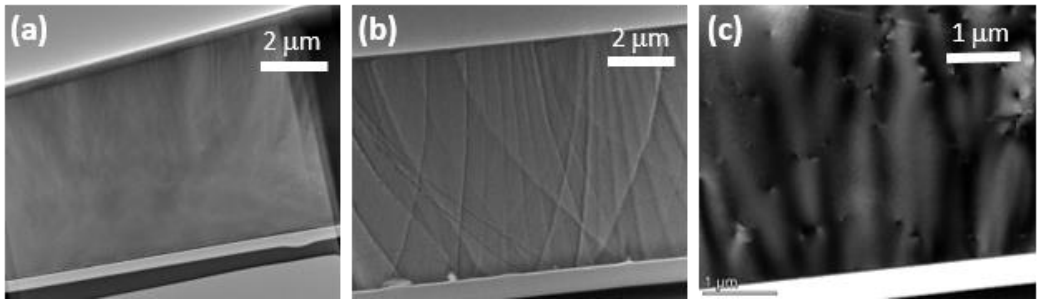

Figure S6: Bright-field TEM data measured on CdS samples: (a) original, (b) vacuum-annealed ("ann. 1"), and (c) sulfur-annealed ("ann. 2"). (c) is shown in higher magnification to make the screw dislocations more evident (the dark/light dipole pattern).

The measured opto-mechanical effects are suppressed with annealing, even as extended defects proliferate. This further supports our hypothesis that the main cause of optomechanical response – and photoelasticity in particular – is ionized point defects.

S6. Photoconductivity and point defect ionization

In materials that exhibit large and persistent photoconductivity, the recombination lifetime of photo-excited carriers can be quite long, on the scale of seconds or longer. The most widely-studied example of this is probably that of DX centers in III-V semiconductors [20]. Large and persistent photoconductivity is also observed in $CuInSe_2$, ZnO, CdS, and likely other compound semiconductors [21–23]. These phenomena were well-captured by semiconductor physics models in "*Photoconductivity of solids*" by Richard Bube (Wiley, 1960) [10]. An atomistic picture to explain the long recombination lifetime (alternatively, reduced capture cross sections) too longer to develop. Lang and Logan in 1977 introduced a large lattice relaxation model to explain DX center persistent photoconductivity [13]. Zhang, Wei, Lany and Zunger later studied similar models in oxide and chalcogenide compounds, using more modern theoretical tools, an effort continued by our more recent work on CdS [21–23]. The unifying theme is that, for certain point defects, ionization is accompanied by lattice relaxations that kinetically trap the non-equilibrium ionization state for an extended period of time; for details, we encourage perusing the cited works. Long excited-state lifetimes enhance the likelihood of defect ionization even for relatively mild illumination conditions. This is the functional basis for very sensitive photodetectors, such as flame detectors used in chemical fume hoods and production facilities, that are based on the extremely-large photoresponse of CdS.

To further support this understanding, in the specific context of the experiments reported here, we performed additional measurements of the photoconductive response of the original CdS crystal. We contacted the crystal using silver epoxy (Bacon Industries LCA-24) and used a white LED (Thorlabs Solis-1A) for illumination. We directly measured the illumination intensity at the sample location using a bolometer. This data, together with information on the output spectrum from the manufacturer, allows us to calculate the spectral intensity seen by the sample. We then combine this illumination intensity spectrum with tabulated data for the absorption coefficient of CdS to numerically calculate the optical generation rate in the CdS sample. For reasons that become clear below, we calculate an area-specific generation rate $\tilde{g}$ (units of photons/cm^2/s) as follows:

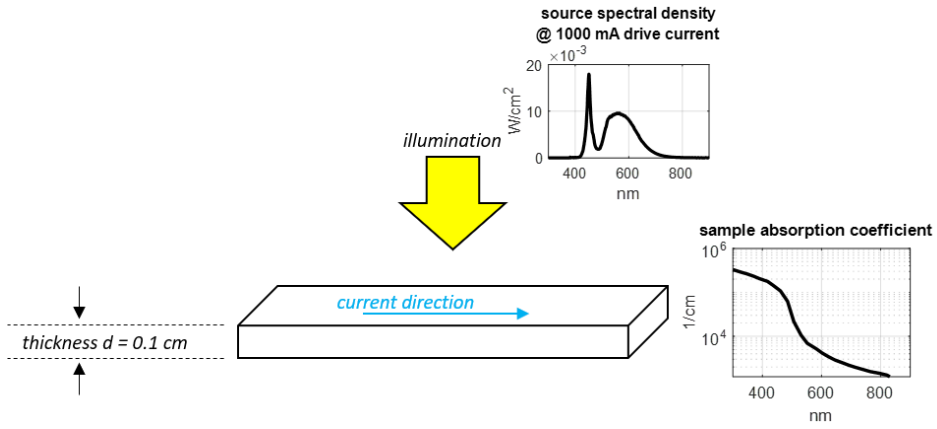

$$\tilde{g} = \int d\lambda I_{ph}(1 - e^{-\alpha d})$$

I_{ph} is the spectral intensity seen by the sample (in of photons/cm^2/s/nm), and α is the absorption coefficient spectrum. The geometry and key input data are presented in **Fig. S7**. In this way, we calculate for instance $\tilde{g} = 1.12 \times 10^{17}$ 1/s/cm^2 for an LED drive current of 1000 mA.

Figure S7: Geometry of crystal photoconductivity measurement, and key input data needed to calculate the optical generation rate.

The electrical measurement is sensitive to the whole sample, of thickness $d = 1$ mm, whereas the optical generation is non-uniform through the thickness. We therefore rearrange Ohm's law and the Drude model as follows:

$$R^{-1} = \frac{q\mu w}{L} nd$$

$$nd = n_0 d + \int_0^d dx \Delta n(x) \equiv n_0 d + \Delta\tilde{n}$$

R is the measured sample resistance. q is the fundamental charge, μ is the mobility, w is the sample width, L is the sample length, and we assume that $\frac{q\mu w}{L}$ is unchanged by illumination. $\Delta n(x)$ is the depth-dependent excess carrier concentration due to illumination, and $\Delta\tilde{n}$ is shorthand for the integral along the depth direction, which is area-specific and has units of cm^{-2}. Our experiments measure $y \equiv R_{\text{light}}^{-1}/R_{\text{dark}}^{-1}$, and we find experimentally that $y \gg 1$. Therefore, we have:

$$y = \frac{R_{\text{light}}^{-1}}{R_{\text{dark}}^{-1}} = \frac{n_0 d + \Delta\tilde{n}}{n_0 d} \approx \frac{\Delta\tilde{n}}{n_0 d}$$

Photo-excited carriers recombine with a time constant τ, which we assume to be a constant throughout the sample. For a given area-specific generation rate $\tilde{g}$, we have a simple rate equation:

$$\dot{\tilde{n}} = \tilde{g} - \tilde{n}/\tau \approx \tilde{g} - \Delta\tilde{n}/\tau$$

This is the most basic rate equation for generation and recombination in a semiconductor, appropriate for a photoconductor. The approximation follows from $y \gg 1$. Solving for the static case $\dot{\tilde{n}} = 0$, we find:

$$\Delta\tilde{n} = \tilde{g}\tau$$

Rearranging and using the above expressions, this becomes:

$$\tau = \frac{y n_0 d}{\tilde{g}}$$

This expression for the recombination lifetime depends on a photoconductivity measurement result (y), the equilibrium carrier concentration (n_0), the sample thickness (d), and the area-specific generation rate ($\tilde{g}$). Of these, only n_0 is unknown. Typical values for CdS crystals range from $10^{13} - 10^{19}$ cm^{-3}; accurate measurement is difficult because of the rather low mobility of CdS, and its extreme light-sensitivity [23].

Using our measured value of $y = 13.4$ (for 1000 mA LED drive current and 1 V supply voltage), we calculate τ for a wide range of n_0, as shown in **Fig. S8**. The results confirm what is expected for semiconductors such as CdS that exhibit large and persistent photoconductivity: the excited-state lifetime is remarkably long, even on the order of seconds or longer.

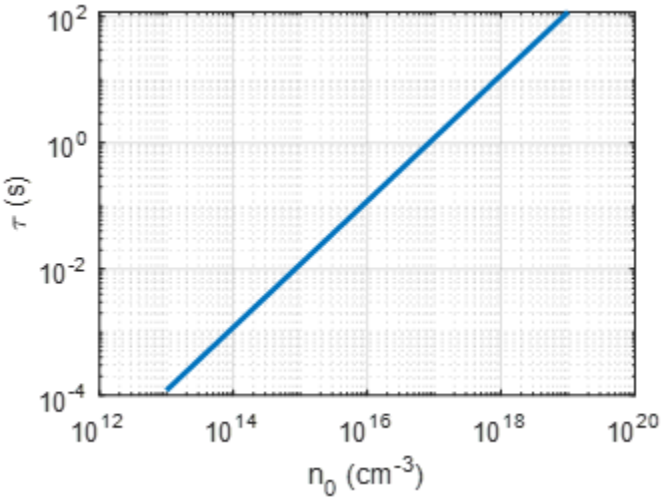

Figure S8: Excited-state lifetime for CdS photoconductivity, calculated for a range of equilibrium carrier concentration (n_0) from measured sample photoresponse.

S7. Calculated elastic tensors

In **Figs. S9-12** we present the elastic tensors calculated for varying sulfur vacancy concentration [V_S] for four different phases. We simulate hexagonal wurtzite CdS, and cubic zinc blende ZnS. We also simulate two unstable phases of CdS: cubic zinc blende, and cubic rock salt. In each case we define DFT simulation volumes of different sizes and shapes, each with one sulfur vacancy, and calculate the stiffness for both the neutral and doubly-ionized configurations. As throughout, [V_S] is expressed as a fraction of vacant sulfur sites.

In all cases, defect ionization increases c_{11} and c_{12}. The shear components c_{44} (and c_{66}, for hexagonal CdS) decrease upon ionization for all but rock salt CdS. In all cases, the elastic tensor component changes upon ionization are large, corresponding to giant photo-elasticity, as observed experimentally.

There are two significant reasons why we do not expect exact correspondence between the theoretically-predicted c_{ij} and the experimentally-measured Young's modulus: one relating to anisotropy, and one relating to inaccuracy of the theoretical methods used. The results here have been averaged to approximately restore the symmetry of the pristine system, as described above (**Sec. S2**). However, the observed anisotropic changes in the lattice upon defect creation and ionization (**Fig. 3**) imply that, in a real-world sample, there is expected a distribution of local lattice configurations around point defects. This distribution could be fully stochastic, which would have a similar averaging effect to that employed here numerically. Alternatively, defects could be correlated through long-range strain interactions. The distribution of defect configurations might also be affected by built-in strain fields (*e.g.* near dislocations), and could be dynamically changed through mechanical forces and deformation, such as during nanoindentation. For instance, the preferred direction of the three-in, one-out pattern observed around neutral sites $V_S^{\times}$ (**Fig. 3a, c**) could interact with applied stress, aligning individual defect distortion patterns and producing large changes in effective modulus. These effects ought to be studies using a coarse-grained field theory, coupled to the atomistic DFT calculations and to

finite-element analysis (FEA) simulation of the nanoindentation process. We leave such to future work.

We also acknowledge that DFT is not yet fully reliable for predicting the properties of extended solids with charged defects. The standard approaches for correcting spurious electrostatic interactions are acknowledged to be not fully reliable [37]. Modeling the elastic properties of solids with neutral and ionized point defects has not yet been well scrutinized by the DFT methods-development community. We leave such to future work.

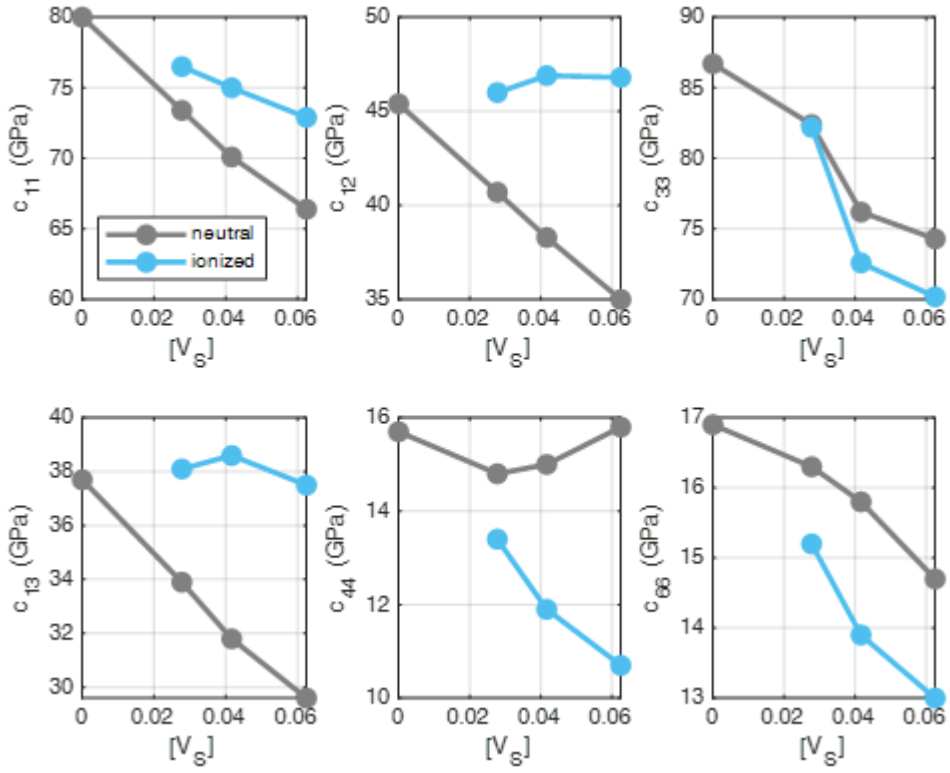

Figure S9: Calculated c_{ij} for hexagonal CdS.

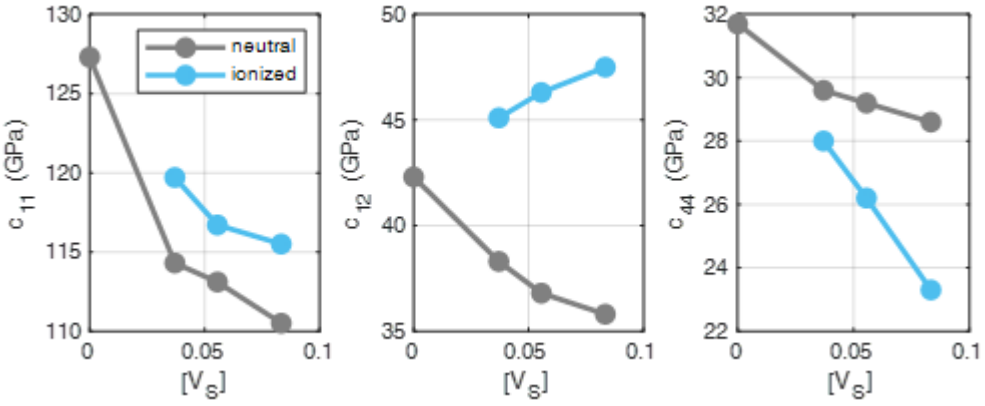

Figure S10: Calculated c_{ij} for ZnS.

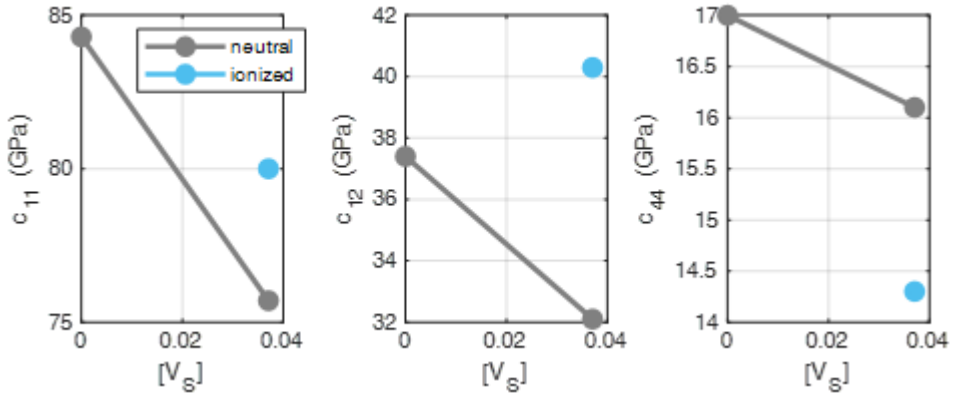

Figure S11: Calculated c_{ij} for cubic zinc blende CdS.

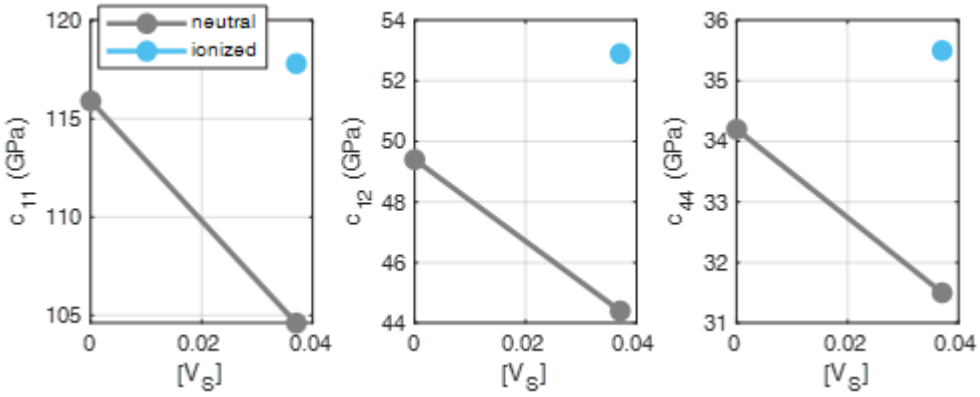

Figure S12: Calculated c_{ij} for cubic rock salt CdS.

S8. Competing theoretical explanations

A competing theoretical explanation for the giant photoelastic response measured by nanoindentation is that the change in the concentration of free charge carriers and/or excitons upon illumination increases the stiffness via photostriction. The photostriction coefficient $\alpha = (\frac{d\varepsilon}{dn})_T = -\frac{1}{3}\left(\frac{dE_g}{dp}\right)_T$ (the latter equation is for isotropic materials) is on the order of $|\alpha| \sim 1 \times 10^{-24}$ cm^3 for

common semiconductors [1,2,13]. Using DFT, we calculate $\alpha = -2.3 \times 10^{-24}$ for CdS. Changes in charge carrier concentration under illumination can be locally enhanced, by the surface photovoltage effect, and by strain gradients created during nanoindentation. Changes to the elastic stiffness on the order of 10% (as experimentally observed here) would require enormous changes in the carrier concentration, on the order of 10^{22} cm^{-3}. Such a large change cannot be produced by the surface photovoltage effect. For completeness, we analyze the contribution of strain gradients during nanoindentation to creating an "exciton funnel", enhancing the local change in charge carrier concentration beyond what would occur for the case of uniform stress and strain [41]. We find that the exciton concentration beneath the nanoindentation tip in CdS reaches a local maximum of 10^{12} cm^{-3}, which is too small by a factor of 10^{10} to explain the experimental results. This estimate relies on a number of assumptions, which do affect the quantitative result but not the conclusions. The excited-state lifetime (τ) is perhaps the most likely to vary widely from sample-to-sample, and it affects the exciton concentration linearly. Here we assume $\tau = 200$ ps. For highly defect-free semiconductors, the excited-state lifetime can exceed 1 μs. However, even a value of $\tau = 1$ ms would leave the photostriction effect orders-of-magnitude too weak to explain experimental results.

In polar materials such as CdS and ZnO, the piezoelectric response arising from the surface photovoltage (SPV) may also contribute to optomechanical effects measured by nanoindentation. We estimate this effect by assuming $V_{\mathrm{SPV}} = 0.1$ V, consistent with experimental reports for CdS [46,47]. For shallow donor density $N_D = 10^{18}$ cm^{-3}, the peak change in electric field is 5×10^3 V/m [48]. Given the piezoelectric coefficient $d_{33} = 10.32 \times 10^{-12}$ V/m for CdS, we find a peak strain on the order of 10^{-7}. We conclude that the piezoelectric effect is a negligible contribution to the measured photoelasticity for CdS. The effect should be even smaller for measurements on a-plane ZnO, and nonexistent for measurements on non-polar ZnS.